ADVANCED MATERIALS
www.advmat.de

Modulation of Spin–Orbit Torque from $SrRuO_3$ by Epitaxial-Strain-Induced Octahedral Rotation

*Jing Zhou, Xinyu Shu, Weinan Lin, Ding Fu Shao, Shaohai Chen, Liang Liu, Ping Yang, Evgeny Y. Tsymbal, and Jingsheng Chen**

Spin–orbit torque (SOT), which arises from the spin–orbit coupling of conduction electrons, is believed to be the key route for developing low-power, high-speed, and nonvolatile memory devices. Despite the theoretical prediction of pronounced Berry phase curvatures in certain transition-metal perovskite oxides, which lead to considerable intrinsic spin Hall conductivity, SOT from this class of materials has rarely been reported until recently. Here, the SOT generated by epitaxial $SrRuO_3$ of three different crystal structures is systematically studied. The results of both spin-torque ferromagnetic resonance and in-plane harmonic Hall voltage measurements concurrently reveal that the intrinsic SOT efficiency of $SrRuO_3$ decreases when the epitaxial strain changes from tensile to compressive. The X-ray diffraction data demonstrate a strong correlation between the magnitude of SOT and octahedral rotation around the in-plane axes of $SrRuO_3$, consistent with the theoretical prediction. This work offers new possibilities of tuning SOT with crystal structures and novel opportunities of integrating the unique properties of perovskite oxides with spintronic functionalities.

Current induced spin–orbit torque (SOT), which arises from the spin–orbit coupling between the electron spin and the orbital angular momentum, has proved to be a subject of strong academic interest and a promising scheme for developing low-power magnetic devices.[1–3] Traditionally, materials generating a large SOT are predominantly semiconductors[4,5] and heavy metals.[3,6,7] Other SOT materials have also been investigated, such as antiferromagnets,[8,9] topological insulators,[10,11] and 2D materials.[12–14] Oxides, which have poor electrical conductivity in general, have remained naturally unexplored in the discipline of SOT until recently. Certain 4d and 5d transition metal oxides, such as $SrIrO_3$ and $SrRuO_3$, exhibit moderate electrical conductivity and strong Berry phase curvatures,[15–17] which give rise to large intrinsic spin Hall conductivity (SHC). Therefore, these oxides are potentially good sourcing materials for SOT.

The transition metal oxides have a multitude of degrees of freedom, such as the crystal lattice, charge, spin, and orbital. These tunable parameters are interconnected with each other and are not always fully accessible in other material classes. The perovskite crystal structure of $SrRuO_3$ has been extensively studied since the rotation of the RuO_6 octahedra has enormous impacts on its electrical and magnetic properties.[18–26] This octahedral rotation is expected to influence SOT as well from two perspectives. First, the band structure of $SrRuO_3$ determines its intrinsic SHC, which is strongly influenced by the octahedral crystal field.[27–30] Second, the octahedral rotation may alter the local inversion symmetry, which has been demonstrated to be crucial for SOT generation.[12,31,32] Therefore, tuning the octahedral rotation represents a distinguished means of modulating SOT since it potentially allows external control of the intrinsic SHC. For instance, it has been demonstrated in a variety of perovskite oxides that the octahedral rotation can be controlled by an electric field.[33–35] This offers greater flexibility in designing full-electric-field-controlled SOT memory devices. In recent studies, sizable SOT has been observed experimentally in both $SrIrO_3$ and $SrRuO_3$.[36–38] Variations of the SOT efficiency with the thickness of $SrIrO_3$ and $SrRuO_3$ were attributed to the thickness-dependent octahedral rotation.[36,38] However, the relation between the octahedral rotation and SOT is still blurred due to limited evidences.

In this work, we investigate the effects of the octahedral rotation on the SOT generated by $SrRuO_3$ above its Curie temperature. By carefully engineering the epitaxial strain, we deposit three types of $SrRuO_3$ thin films with different octahedral rotations. We examine the SOT in $SrRuO_3/Ni_{81}Fe_{19}$ [also referred as Permalloy (Py)] bilayer using both spin-torque ferromagnetic resonance (ST-FMR) and in-plane harmonic Hall voltage (HHV) techniques. The results from the two techniques agree

Dr. J. Zhou, X. Shu, Dr. W. Lin, Dr. S. Chen, Dr. L. Liu, Dr. P. Yang, Prof. J. Chen
Materials Science and Engineering
National University of Singapore
9 Engineering Drive 1, Singapore 117575, Singapore
E-mail: msecj@nus.edu.sg

Dr. D. F. Shao, Prof. E. Y. Tsymbal
Department of Physics and Astronomy and Nebraska Center for Materials and Nanoscience
University of Nebraska
Lincoln, NE 68588, USA

Dr. P. Yang
Singapore Synchrotron Light Source (SSLS)
National University of Singapore
5 Research Link, Singapore 117603, Singapore

The ORCID identification number(s) for the author(s) of this article can be found under https://doi.org/10.1002/adma.202007114.

DOI: 10.1002/adma.202007114

 © 2021 Wiley-VCH GmbH

with each other. Relatively larger SOT efficiencies are observed in $SrRuO_3$ thin films under a large tensile strain or a small compressive strain, which correspond to octahedral rotations around the in-plane axes of $SrRuO_3$. By contrast, such octahedral rotations are absent for $SrRuO_3$ thin films under a large compressive strain, where negligible SOT is generated. Furthermore, we find that the SOT efficiencies of $SrRuO_3$ decrease rapidly with increasing temperature (decreasing electrical conductivity). This suggests the dominant contribution to SOT in $SrRuO_3$ is the intrinsic SHC in the "dirty metal" regime[36,39] and therefore supports the influence of the octahedral rotation.

Bilayers of $SrRuO_3$ (10, 20 nm)/Py(4 nm) are prepared using pulsed laser deposition and DC magnetron sputtering (see the Experimental Section). Taking into account the lattice mismatch with bulk $SrRuO_3$, we choose three different single-crystal substrates, namely, $NdGaO_3$ $(001)_c$ (the "c" in the subscript denotes pseudocubic lattice), $SrTiO_3$ (001) and $KTaO_3$ (001) (hereby referred as NGO, STO, and KTO). Their bulk lattice constants (a) take the following order: $a_{NGO} < a_{STO} < a_{SrRuO_3} < a_{KTO}$. In our previous reports,[18,40] we found that the large compressive strain from NGO enhances (suppresses) the octahedral rotation about the out-of-plane (in-plane) axis of $SrRuO_3$. By contrast, a large tensile strain from KTO stretches the network of octahedra and induces substantial octahedral rotation around the in-plane axes of $SrRuO_3$. In the case of STO, a small compressive strain results in an intermediate structure between the two extremes. **Figure 1**a schematically illustrates the effects of epitaxial strain on the lattice parameters of $SrRuO_3$.

We first examine the crystal structures of the epitaxial $SrRuO_3$ thin films using X-ray diffraction (XRD). The $\theta - 2\theta$ scans that probe along the [00L] direction in reciprocal space are shown in Figure 1b. For all three curves, all peaks from the $\{001\}_c$ family of the bulk $SrRuO_3$ crystal but no other film peaks are observed in the diffraction pattern. This indicates good crystallinity and $(001)_c$ epitaxy of the $SrRuO_3$ films on all substrates. The inset shows an enlarged view of a representative $(002)_c$ film peak with Laue oscillation, which further confirms the high crystallinity. Two tests are performed to verify the epitaxial relations in the film plane. Figure 1c shows a typical ϕ-scan. Both the substrates and the film exhibit a fourfold symmetry of the 103 peak indicating only a negligible phase difference between the substrate and the film peaks. This suggests that the epitaxial relation of substrate/$SrRuO_3$ is $[100]/[100]_c$. The typical reciprocal space mappings (RSMs) around (103) are shown in Figure 1d. For all three substrates, the film and substrate have similar H values. This verifies the epitaxial relation derived by the ϕ-scan and also suggests that our $SrRuO_3$ films are almost fully strained. Based on the reciprocal space vectors,[41] we extract the lattice constants of $SrRuO_3$ as follows: $a = b = 3.989$ Å and $c = 3.898$ Å for KTO/$SrRuO_3$; $a = 3.917$ Å, $b = 3.933$ Å and $c = 3.946$ Å for STO/$SrRuO_3$; $a = b = 3.850$ Å and $c = 4.013$ Å for NGO/$SrRuO_3$. All angles between the unit cell sides are measured to be 90° within experimental error, except β for $SrRuO_3$ on STO, which is 89.6°, as indicated in Figure 1a. It is worth noting that lattice parameters alone are insufficient to determine the structural phase of $SrRuO_3$ when an octahedral rotation is present, since the octahedral rotation can lower the symmetry derived from lattice parameters.

The SOT in the $SrRuO_3$/Py bilayers is evaluated using the ST-FMR technique at room temperature[3,9,31] (see the Experimental Section; Note S1 of the Supporting Information for details). **Figure 2**a shows the schematic setup, where

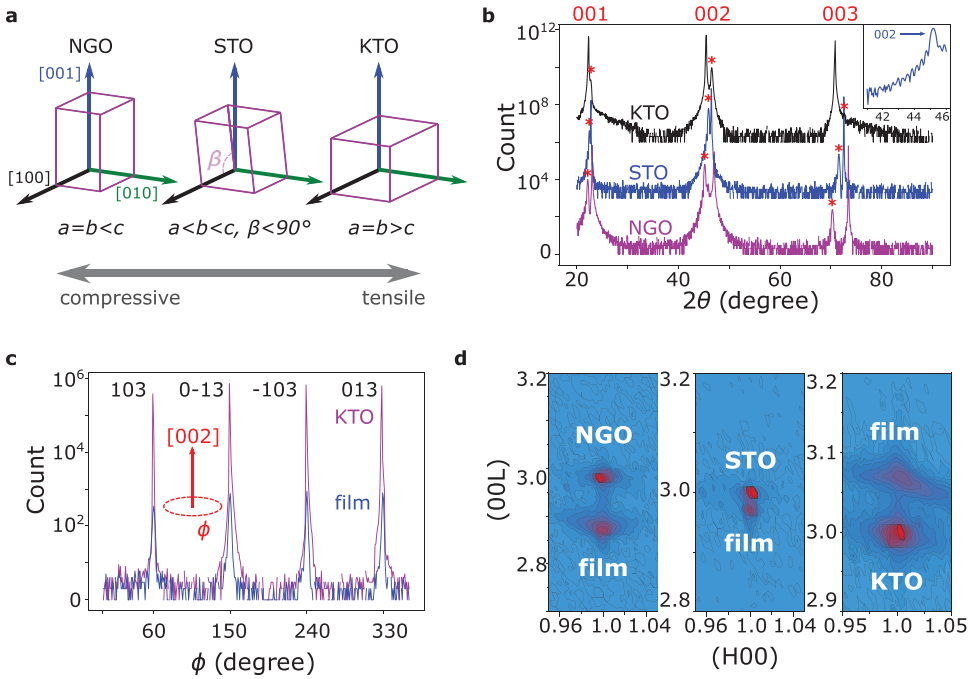

Figure 1. Epitaxial growth of $SrRuO_3$ thin films. a) Schematic illustration of the effects of epitaxial strain on the lattice parameters of $SrRuO_3$. The coordinates are labeled as mutually orthogonal in pseudocubic lattice. b) $\theta - 2\theta$ scans that probe along [00L] direction in reciprocal space. Film peaks are labelled with "*". The inset shows an enlarged picture of 002 peak of $SrRuO_3$ on STO. Arbitrary back grounds are added separate the plots. c) ϕ scan of KTO/$SrRuO_3$. d) RSMs around (103) of $SrRuO_3$ films on different substrates.

 © 2021 Wiley-VCH GmbH

15214095, 2021, 30, Downloaded from https://advanced.onlinelibrary.wiley.com/doi/10.1002/adma.202007114 by Westlake University, Wiley Online Library on [16/10/2026]. See the Terms and Conditions (https://onlinelibrary.wiley.com/terms-and-conditions) on Wiley Online Library for rules of use; OA articles are governed by the applicable Creative Commons License

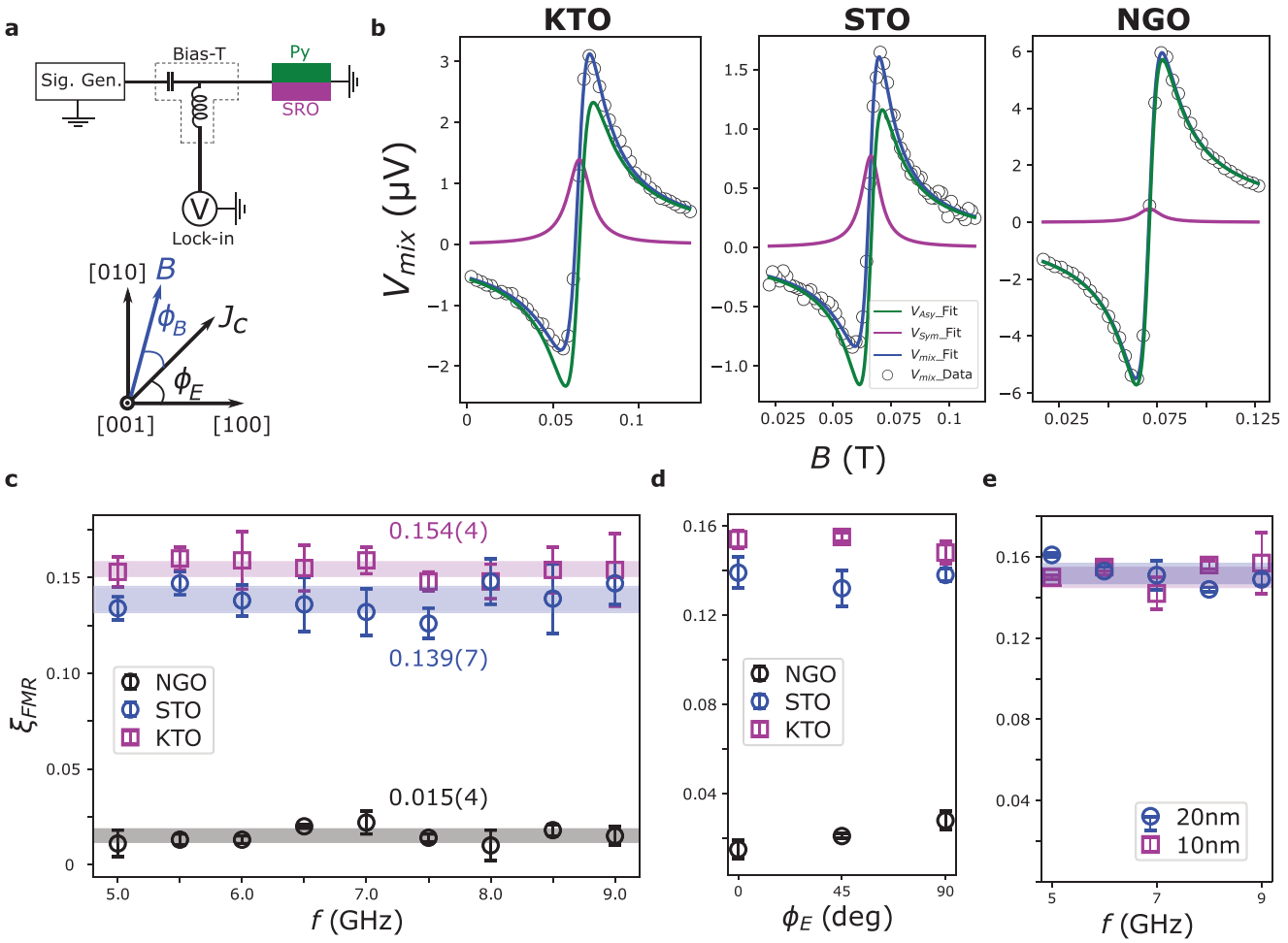

Figure 2. SOT efficiency (ξ_{FMR}) measured by ST-FMR. a) Schematic setup. The coordinate system is based on the crystal lattice of the $SrRuO_3$ film. b) Measured ST-FMR voltage (V_{mix}) at 7 GHz from $SrRuO_3$ (20 nm)/Py (4 nm) bilayer deposited on different substrates. $\phi_B = 45°$ and $\phi_E = 0°$. c) ξ_{FMR} from 5 to 9 GHz with the microwave direction $\phi_E = 0°$. d) Dependence of ξ_{FMR} on ϕ_E measured at $\phi_B = 45°$. e) Dependence of ξ_{FMR} on the $SrRuO_3$ thickness in KTO/$SrRuO_3$/Py. The shaded regions in (c,e) indicate average values within 1 standard deviation (s.d.).

a rectifying voltage V_{mix} is measured when a microwave J_c is applied to the bilayer under external in-plane magnetic field B. V_{mix} has a symmetric component (V_{sym}) with the amplitude V_S and an antisymmetric component (V_{asy}) with the amplitude V_A. The merit of ST-FMR is its self-calibrating nature, which allows comparison of the relative change in damping-like SOT efficiency (ξ_{FMR}) using the ratio V_S/V_A

$$\xi_{FMR} = \frac{V_S}{V_A}\frac{e\mu_0 M_s d_{SRO} d_{Py}}{\hbar}\sqrt{1+\frac{\mu_0 M_{eff}}{B_{res}}} \quad (1)$$

Here, e is the electron charge, μ_0 is the permeability of free space, $\hbar$ is the reduced Planck constant, and B_{res} is the resonant field. The thicknesses of the two layers are d_{SRO} and d_{Py}, respectively. The saturation magnetization and the effective in-plane magnetization of the Py layer are M_s and M_{eff}, respectively.

Typical spectra of V_{mix} and its components measured at 7 GHz with field direction $\phi_B = 45°$ are shown in Figure 2b. An obvious symmetric component is observed for $SrRuO_3$/Py deposited on both KTO and STO substrates, which indicates a substantial amount of damping-like SOT. By contrast, the symmetric component is negligibly small for $SrRuO_3$/Py on NGO, which corresponds to a much smaller damping-like SOT. Figure 2c shows the ξ_{FMR} measured at different frequencies. The average ξ_{FMR} across the frequency range for $SrRuO_3$/Py on the KTO, STO, and NGO substrates are 0.154, 0.139, and 0.015, respectively. The values of ξ_{FMR} for the bilayers deposited on KTO and STO are similar to that for the orthorhombic $SrRuO_3$/Co bilayer measured by ST-FMR.[36] We verify that the variations in ξ_{FMR} across three substrates are not likely to be caused by differences in the longitudinal electrical resistivity ρ_{xx} of the $SrRuO_3$ layers, which are 174.7 μΩ cm (KTO), 120.5 μΩ cm (STO), and 114.3 μΩ cm (NGO), respectively (see Note S2, Supporting Information).

We modify parameters of our ST-FMR measurement to further investigate the physical significance of the observed ξ_{FMR}. In Figure 2d, ξ_{FMR} appears to be roughly independent of the microwave direction (ϕ_E) relative to the $SrRuO_3$ lattice for all three substrates. This implies that the intrinsic spin Hall conductivities of $SrRuO_3$ in all its three phases are more or less isotropic, as opposed to $SrIrO_3$.[15,37,38] Another possibility is the twinned crystal domains, which has been reported frequently

 © 2021 Wiley-VCH GmbH

15214095, 2021, 30, Downloaded from https://advanced.onlinelibrary.wiley.com/doi/10.1002/adma.202007114 by Westlake University, Wiley Online Library on [16/10/2026]. See the Terms and Conditions (https://onlinelibrary.wiley.com/terms-and-conditions) on Wiley Online Library for rules of use; OA articles are governed by the applicable Creative Commons License

in $SrRuO_3$[36,42] and other materials.[9] This would flatten the in-plane anisotropy of SOT in measurement, even it exists intrinsically. It has been reported that the measured SOT efficiencies are affected by many thickness-dependent mechanisms, such as spin diffusion length,[8] electrical resistivity,[31] and crystal phase.[36,38] We find that the thickness of the $SrRuO_3$ layer in this study is sufficiently large to have a notable effect on ξ_{FMR}. As seen from Figure 2e, there is almost no change in ξ_{FMR} when $SrRuO_3$ thickness in KTO/$SrRuO_3$/Py is reduced from 20 to 10 nm. This is consistent with the previous reports[36,38] and therefore we expect the crystal structure of $SrRuO_3$ to remain unchanged for both film thicknesses investigated here. Also, for $SrRuO_3$ film thickness of 10 nm and above, the electrical resistivity [31] and spin diffusion length[8] should be saturated. In addition, we measure the V_{mix} at varying external field direction ϕ_B, which is shown in Note S3 of the Supporting Information. Both V_{sym} and V_{asy} have only the $\sin(2\phi_B)\cos(\phi_B)$ component, suggesting the regular in-plane damping-like and out-of-plane field-like SOT. The only magnetic anisotropy in our $SrRuO_3$/Py samples is a small (≈1.5 mT) in-plane uniaxial anisotropic field, which is consistent with the previous report on Py.[43]

The SOT efficiency extracted by the ratio analysis represents the relative strength of in-plane damping-like torque to out-of-plane field-like torque, where the latter has been assumed to be of a predominant Oersted origin in metals.[3,6,7] However, it is unclear if this assumption holds for oxides. We conduct two experiments to address this question. First, we measure the dampinglike SOT efficiency $\xi_{DL,\ FMR}$ using the DC-tuned ST-FMR technique (Note S4, Supporting Information). The results suggest that the SOT generated by $SrRuO_3$ is predominantly damping-like. Second, we use the in-plane HHV technique[12,44–46] to measure the SOT efficiency in $SrRuO_3$ (20 nm)/Py (4 nm) independently, where the SOT efficiency is extracted from the damping-like torque only (see the Experimental Section; Note S5 of the Supporting Information for details). **Figure 3**a shows a schematic setup of the HHV measurement. The second harmonic Hall resistance $R_{xy}^{2\omega}$ in response to an alternating current $J_c\sin(\omega t)$ is measured while an in-plane external magnetic field B applied at an angle ϕ_B with J_c. The measured $R_{xy}^{2\omega}$ is fitted against ϕ_B using

$$R_{xy}^{2\omega} = \frac{R_{PHE}\tau_{FL}}{\gamma B}\cos(2\phi_B)\cos(\phi_B) + \left[\frac{R_{AHE}\tau_{DL}}{2\gamma(B+\mu_0 M_{eff})} + R_{ANE}\right]\cos(\phi_B) + R_x\sin(2\phi_B) \quad (2)$$

Here R_{PHE}, R_{AHE}, and γ are the planar Hall resistance, the anomalous Hall resistance, and the gyromagnetic ratio, respectively. The $\cos(2\phi_B)\cos(\phi_B)$ term describes the strength of field-like SOT (τ_{FL}). The $\cos(\phi_B)$ term consists of contributions from both the damping-like torque (τ_{DL}) and the anomalous Nernst effect (R_{ANE}). The $\sin(2\phi_B)$ term with amplitude R_x, which has been removed during data processing or sometimes ignored in previous studies, is likely to arise from a thermal gradient along the direction of current[45] (Note S6, Supporting Information). Figure 3b shows the typical $R_{xy}^{2\omega}$, which can be well fitted using Equation (2). After removing the constants from the amplitude of the $\cos(\phi_B)$ term, we plot $\frac{\tau_{DL}}{B+\mu_0 M_{eff}}$ against $\frac{1}{B+\mu_0 M_{eff}}$ to extract the τ_{DL} from the gradient of the linear fit. In Figure 3c, the good linear relation for both devices on KTO and STO is the direct evidence of a sizable damping-like SOT at room temperature (300 K). On the other hand, the same plot for a device on NGO is rather scattered in a small range of $\frac{\tau_{DL}}{B+\mu_0 M_{eff}}$ across the same span of $\frac{1}{B+\mu_0 M_{eff}}$ as those on KTO and STO. This indicates that a negligible damping-like SOT is generated from NGO/$SrRuO_3$. The damping-like SOT efficiency can be computed using $\xi_{DL,HHV} = \frac{2e\tau_{DL}M_s d_{Py}}{\hbar\gamma J_{SRO}}$,[45] where J_{SRO} is the current density in the $SrRuO_3$ layer. We find $\xi_{DL,HHV}$ = 0.078, 0.035, and 0.008 at room temperature for $SrRuO_3$/Py KTO, STO, and NGO, respectively. This is consistent with the order of magnitude of ξ_{FMR}. The numerical discrepancies between $\xi_{DL,HHV}$ and ξ_{FMR} for the same sample are not fully understood at this stage, but have been prevalent in the previous studies as well.[45,47] The possible contributing factors are discussed in Note S7 of the Supporting Information. In Note S8 of the Supporting Information, we also evaluate that the observed differences in $\xi_{DL,HHV}$ and ξ_{FMR} across substrates are less likely to arise from the interface of $SrRuO_3$/Py, though oxidation of Py[48] might influence the interfacial transparency[36,49] of $SrRuO_3$/Py.

In order to interpret the origin of SOT generated by $SrRuO_3$, we examine the temperature (T) dependence of $\xi_{DL,HHV}$. The lowest temperature we present here is 180 K, which is sufficiently higher than the Curie temperature of all phases of $SrRuO_3$.[18,37,40] This ensures that magnetic moments contributing to the HHV measurement are predominantly from Py. Otherwise, the magnetic moments of ferromagnetic $SrRuO_3$ would complicate the signal and physical significance through mechanisms like magnetic inhomogeneity and spin-dependent scattering. In Figure 3d, both the $\xi_{DL,HHV}$ measured from KTO/$SrRuO_3$/Py and STO/$SrRuO_3$/Py are sizable and increase with decreasing T whereas the $\xi_{DL,HHV}$ for the case of NGO/$SrRuO_3$/Py is negligibly small and is almost independent of T. Assuming a spin Hall effect dominated SOT, we compute the effective SHC $\sigma_s = \frac{\xi_{DL,HHV}}{\rho_{xx}}$. Figure 3e summarizes the dependence of σ_s on both T and longitudinal electrical conductivity (σ_{xx}). σ_s shares the similar trend as $\xi_{DL,HHV}$ and its relative strength across substrates does not change with T. Since σ_s of $SrRuO_3$ deposited on both KTO and STO decreases rapidly with increasing T and decreasing σ_{xx}, it closely resembles the intrinsic SHC in the "dirty metal" regime.[36,39] In this scenario, the intrinsic contribution dominates the SHC and it decreases quickly with decreasing carrier mean lifetime τ, which can be gauged by measuring σ_{xx} since $\sigma_{xx} \propto \tau$.

Combining the results from ST-FMR and HHV measurements, we obtain the following implications. First, the SOT generated by $SrRuO_3$ is heavily influenced by its crystal structure, where KTO/$SrRuO_3$ produces the largest amount of SOT followed by STO/$SrRuO_3$, but NGO/$SrRuO_3$ produces negligible SOT. Second, the SOT is likely to arise from the intrinsic mechanism (Figure 3e) with a bulk-like behavior (Figure 2e). In an attempt to understand how the crystal structure of $SrRuO_3$ could possibly affect its SOT, we determine the type of octahedral rotation in different phases by examining half-integer

© 2021 Wiley-VCH GmbH

15214095, 2021, 30, Downloaded from https://advanced.onlinelibrary.wiley.com/doi/10.1002/adma.202007114 by Westlake University, Wiley Online Library on [16/10/2026]. See the Terms and Conditions (https://onlinelibrary.wiley.com/terms-and-conditions) on Wiley Online Library for rules of use; OA articles are governed by the applicable Creative Commons License

peaks from XRD measurement.[18,40,50] A vector $\boldsymbol{g}^*$ in the reciprocal space of unit vector $\boldsymbol{a}^*$, $\boldsymbol{b}^*$, and $\boldsymbol{c}^*$ can be expressed as $\boldsymbol{g}^* = H\boldsymbol{a}^* + K\boldsymbol{b}^* + L\boldsymbol{c}^*$. The half-integer measurements are performed in the coordinate system of the substrates with fixed H and K values but varying L, which we refer as L scan here. **Figure 4**a shows the L scans along selected directions for NGO/$SrRuO_3$. The absence of the (0, 1/2, L) film peaks implies the absence of a^+ rotation. The absence of the (1/2, 1/2, L) film peaks implies the absence of a^-, b^-, and c^+ rotations. The presence of the (1/2, 3/2, 3/2) peak implied the presence of either b^- or c^- rotation. Therefore, the combined results from Figure 4a imply that the octahedral rotation for $SrRuO_3$ on NGO is $a^0a^0c^-$. Here, "a", "b", and "c" denote the axis of rotation; "+", "−", and "0" on the superscript indicate in-phase, out-of-phase, and no octahedral rotation, respectively. In Figure 4b, the presence of the (0, 1/2, 2) peak indicates the presence of b^+ rotation, which also excludes the b^- rotation. The presence of the (1/2, 1/2, 3/2) peak suggests the presence of either a^- or b^- rotation. The presence of the (1/2, 3/2, 3/2) peak indicates either b^- or c^-. Therefore, the octahedral rotation of $SrRuO_3$ on STO substrate is $a^-b^+c^-$. In Figure 4c, similar to the other two substrates, it can be shown that either a^-, b^- or c^- and/or the combination of them is present. Considering the present film peaks are consistent with the previous studies[18,51] and the allowed space group, the octahedral rotation of $SrRuO_3$ on KTO is determined to be $a^-a^-c^+$. Note that this type of octahedral rotation can also be labeled as $a^+c^-c^-$, depending on the orientation of the c-axis of the orthorhombic lattice. [42,51] The combined results of the lattice

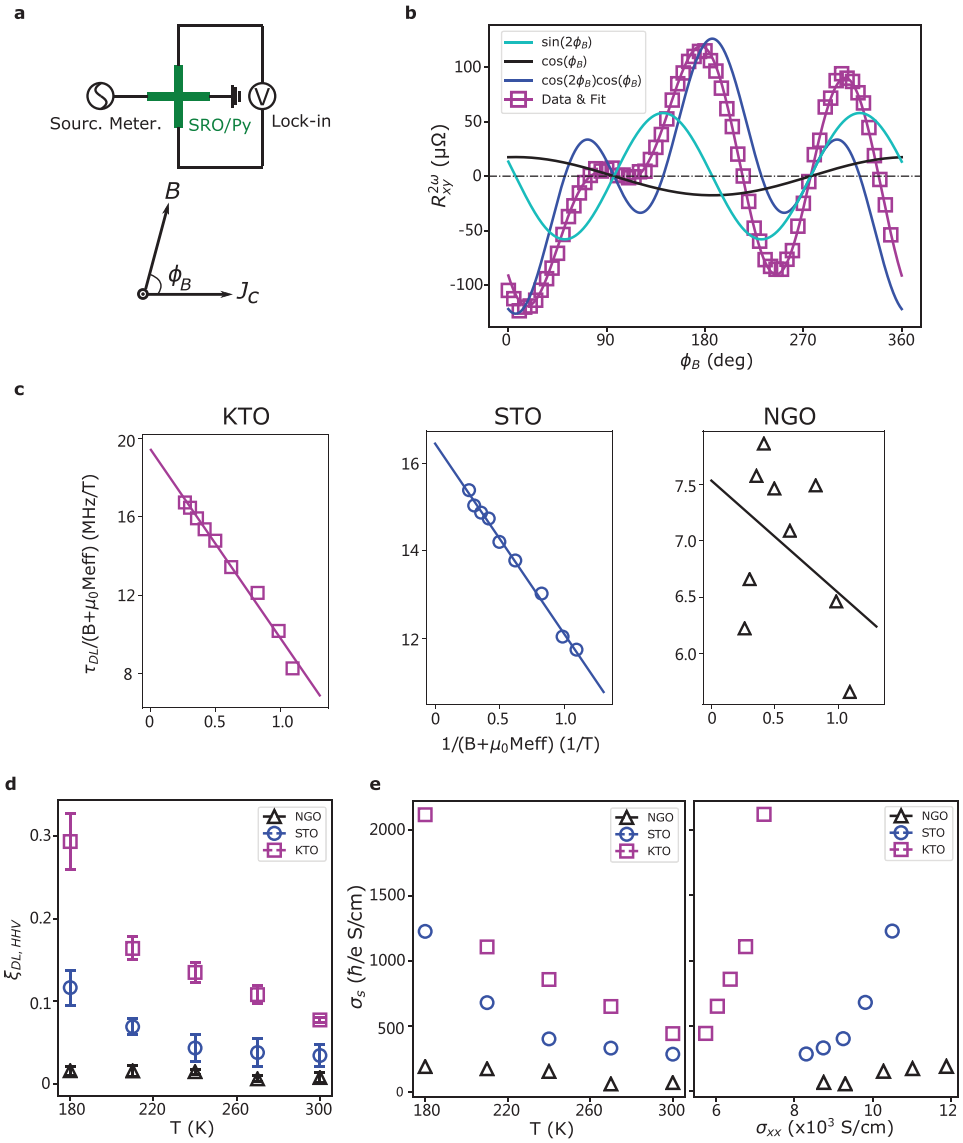

Figure 3. SOT evaluated by HHV technique. a) Schematic setup. b) Typical second harmonic Hall resistance ($R_{xy}^{2\omega}$) at J_c = 8 mA and B = 0.1 T using NGO/$SrRuO_3$/Py at room temperature. c) Linear plot of $\frac{\tau_{DL}}{B+\mu_0 M_{eff}}$ against $\frac{1}{B+\mu_0 M_{eff}}$ for $SrRuO_3$/Py deposited on different substrates. d) Extracted SOT efficiency ($\xi_{DL, HHV}$) at different temperature (T). e) Dependence of effective SHC (σ_s) on T (left) and longitudinal electrical conductivity (σ_{xx}) (right).

 © 2021 Wiley-VCH GmbH

15214095, 2021, 30, Downloaded from https://advanced.onlinelibrary.wiley.com/doi/10.1002/adma.202007114 by Westlake University, Wiley Online Library on [16/10/2026]. See the Terms and Conditions (https://onlinelibrary.wiley.com/terms-and-conditions) on Wiley Online Library for rules of use; OA articles are governed by the applicable Creative Commons License

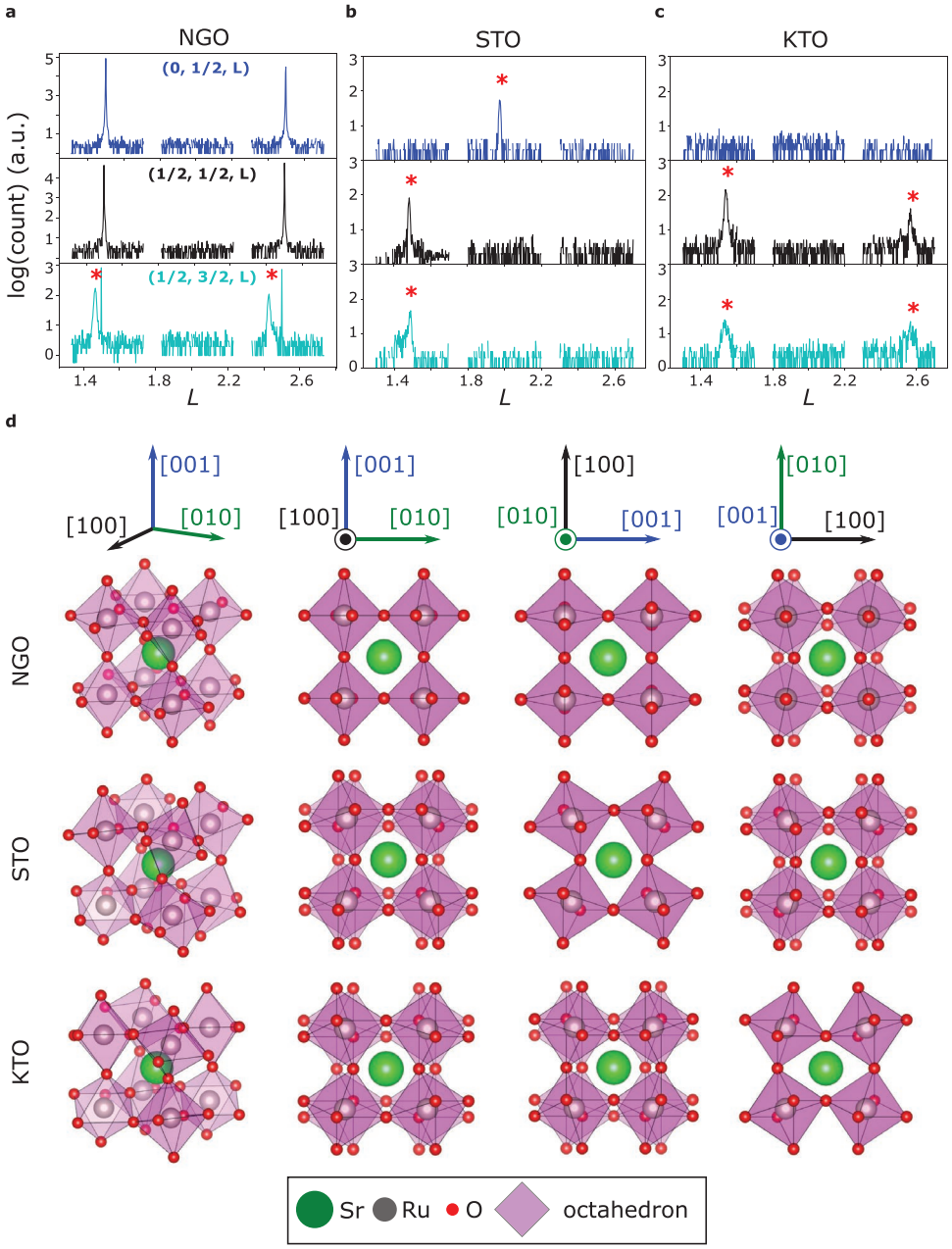

Figure 4. Octahedral rotation in $SrRuO_3$ of different crystal structures. a–c) *L* scans along selected directions for $SrRuO_3$ deposited on different substrates. Film peaks are indicated by "*". The six sharp and narrow peaks in (a) arise from the NGO substrate. The measurement coordinates are defined with reference to the lattice of the substrates. d) Octahedral rotation in $SrRuO_3$ deposited on KTO, STO, and NGO substrate. Coordinates are defined with reference to the pseudocubic lattice of $SrRuO_3$.

parameters and the types of octahedral rotation also allow us to determine the crystal structure $SrRuO_3$. Our $SrRuO_3$ thin films are tetragonal, monoclinic, and orthorhombic when deposited on NGO, STO, and KTO substrates, respectively (Note S9, Supporting Information).

The types of octahedral rotation in $SrRuO_3$ on each substrate are schematically shown in Figure 4d. We find that the $SrRuO_3$ thin film has no octahedral rotation (a^0) around the in-plane axes when depositing on NGO, where minimum SOT efficiencies (ξ_{FMR} and $\xi_{DL,HHV}$) are observed. By contrast, relatively larger SOT efficiencies are correlated to the presence of both in-phase (b^+) and out-of-phase (a^-) octahedral rotations around the in-plane axes of $SrRuO_3$ deposited on STO and KTO substrates. This is consistent with the previous theoretical studies.[15,30] It has been predicted[30] that in a transition metal oxide like $SrRuO_3$, the distortion of the octahedral crystal field due to octahedral rotation splits the e_g and t_{2g} manifolds into sub-bands, where an overlap between the manifolds or sub-bands is supported by the effect of spin–orbit coupling. This counters the dampening effect of a strong crystal field on the spin Hall

 © 2021 Wiley-VCH GmbH

15214095, 2021, 30, Downloaded from https://advanced.onlinelibrary.wiley.com/doi/10.1002/adma.202007114 by Westlake University, Wiley Online Library on [16/10/2026]. See the Terms and Conditions (https://onlinelibrary.wiley.com/terms-and-conditions) on Wiley Online Library for rules of use; OA articles are governed by the applicable Creative Commons License

effect and results in substantially enhanced intrinsic SHC. In our study, owning to the smallest lattice mismatch between STO and $SrRuO_3$, an intermediate crystal structure of $SrRuO_3$ is produced, where an intermediate octahedral rotation is also expected. It is therefore not surprising that the SOT efficiency of $SrRuO_3$ deposited on STO is always between those from the other two substrates, regardless of the measurement method.

To verify the effect of octahedral rotations, we perform first-principles calculations on the intrinsic SHC in bulk $SrRuO_3$ under different strain conditions (see Note S10, Supporting Information). Using the same type of octahedral rotations and the same lattice parameters as experimentally found, we calculate the values of SHC for $SrRuO_3$ on KTO and STO substrates to be much larger than the value of SHC for $SrRuO_3$ on NGO substrate (Figure S9a, Supporting Information). In Figure S11 of the Supporting Information, we show that the calculated intrinsic spin Hall conductivity increases with the angle of octahedral rotation. These results are consistent with our experimental observations indicating that the type and magnitude of the octahedral rotation in $SrRuO_3$ plays a decisive role in controlling the SHC. While changes in the lattice volume also affect the SHC (Figure S10, Supporting Information), they solely cannot explain the experimentally observed SOT efficiencies.

In summary, we have investigated the SOT efficiencies of perovskite oxide $SrRuO_3$ in three crystal structures determined by epitaxial growth of $SrRuO_3$ thin films on different substrates. Using two complementary techniques, spin-torque ferromagnetic resonance and in-plane harmonic Hall voltage measurements, we find that the measured SOT efficiencies of the $SrRuO_3$/Py bilayer deposited on KTO, STO, and NGO substrates at room temperature are ξ_{FMR} = 0.154, 0.139, and 0.015, and $\xi_{DL,HHV}$ = 0.078, 0.035, and 0.008, respectively. The relative strength of $\xi_{DL,HHV}$ does not change when lowering the temperature to 180 K. Dependence of the σ_s on T and σ_{xx} suggests that the dominant contribution to the SOT generated by $SrRuO_3$ is the intrinsic SHC in the "dirty metal" regime. By examining the types of octahedral rotation, we find that the strength of SOT in $SrRuO_3$ is strongly correlated to the octahedral rotation around its in-plane axes.

Experimental Section

Sample Fabrication: The $SrRuO_3$ layer was deposited using a pulsed laser deposition system at 750 °C and under an oxygen pressure of 150 mTorr. They were cooled down to room temperature before transferring in situ to an interconnected sputtering chamber. Then the Py layer was deposited at room temperature using DC magnetron sputtering method with a base pressure of less than 2×10^{-8} Torr. All samples were passivated by a 2 nm SiO_2 layer using RF magnetron sputtering. The $SrRuO_3$/Py bilayer was patterned into microstrip and 6-terminal Hall bar devices by the combination of photolithography and ion beam etching. The microstrip device for ST-FMR measurement has a dimension of 10 µm × 40 µm. The Hall bar device has a width of 10 µm and Hall lead width of 5 and 40 µm between Hall leads. Both types of devices are terminated by a thick electrode of Ti (5 nm)/Cu (100 nm).

Structural Characterization: All of the X-ray diffraction measurements were performed at room temperature at the Singapore Synchrotron Light Source with an X-ray wavelength of 1.541 Å (Cu K_α radiation).

Measurement of SOT: A Rohde & Schwarz SMB 100A signal generator was used to provide the modulated microwave for ST-FMR measurement. The microwave has the frequency of 5–9 GHz, a modulation frequency of 317.3 Hz and a nominal power of 18 dBm. The rectifying voltage was collected using a Zurich Instrument MFLI lock-in amplifier. A Keithley 6221 source meter was used to generate AC current of 317.3 Hz for the HHV measurement. The current amplitude for the data in the main text is 8 mA, which is equivalent to 3.3×10^6 A cm^{-2}. The first and second harmonic Hall voltages were collected using the same lock-in amplifier above.

Supporting Information

Supporting Information is available from the Wiley Online Library or from the author.

Acknowledgements

J.Z., X.S., and W.L. contributed equally to this work. The research was supported by the Singapore Ministry of Education MOE2018-T2-2-043, A*STAR Grant No. A1983c0036, A*STAR IAF-ICP 11801E0036, and MOE Tier1 R-284-000-195-114. J.C. is a member of the Singapore Spintronics Consortium (SG-SPIN).

Conflict of Interest

The authors declare no conflict of interest.

Data Availability Statement

The data that support the findings of this study are available from the corresponding author upon reasonable request.

Keywords

ferromagnetic resonance, octahedral rotation, oxide spintronics, spin–orbit torque, $SrRuO_3$

Received: October 19, 2020
Revised: March 30, 2021
Published online: June 19, 2021

[1] A. Manchon, J. Železný, I. M. Miron, T. Jungwirth, J. Sinova, A. Thiaville, K. Garello, P. Gambardella, *Rev. Mod. Phys.* **2019**, *91*, 035004.
[2] A. Manchon, S. Zhang, *Phys. Rev. B* **2008**, *78*, 212405.
[3] L. Liu, T. Moriyama, D. C. Ralph, R. A. Buhrman, *Phys. Rev. Lett.* **2011**, *106*, 036601.
[4] D. Fang, H. Kurebayashi, J. Wunderlich, K. Vyborny, L. P. Zarbo, R. P. Campion, A. Casiraghi, B. L. Gallagher, T. Jungwirth, A. J. Ferguson, *Nat. Nanotechnol.* **2011**, *6*, 413.
[5] M. O. A. Chernyshov, X. Liu, J. K. Furdyna, Y. Lyanda-Geller, L. P. Rokhinson, *Nat. Phys.* **2009**, *5*, 656.
[6] L. Liu, C.-F. Pai, Y. Li, H. W. Tseng, D. C. Ralph, R. A. Buhrman, *Science* **2012**, *336*, 555.
[7] C. Pai, L. Liu, Y. Li, H. W. Tseng, D. C. Ralph, R. A. Buhrman, *Appl. Phys. Lett.* **2012**, *101*, 122404.
[8] W. Zhang, M. B. Jungfleisch, W. Jiang, J. E. Pearson, A. Hoffmann, F. Freimuth, Y. Mokrousov, *Phys. Rev. Lett.* **2014**, *113*, 196602.

 © 2021 Wiley-VCH GmbH

15214095, 2021, 30, Downloaded from https://advanced.onlinelibrary.wiley.com/doi/10.1002/adma.202007114 by Westlake University, Wiley Online Library on [16/10/2026]. See the Terms and Conditions (https://onlinelibrary.wiley.com/terms-and-conditions) on Wiley Online Library for rules of use; OA articles are governed by the applicable Creative Commons License

[9] J. Zhou, X. Wang, Y. Liu, J. Yu, H. Fu, L. Liu, S. Chen, J. Deng, W. Lin, X. Shu, H. Y. Yoong, T. Hong, M. Matsuda, P. Yang, S. Adams, B. Yan, X. Han, J. S. Chen, *Sci. Adv.* **2019**, *5*, 6696.
[10] Y. Fan, P. Upadhyaya, X. Kou, M. Lang, S. Takei, Z. Wang, J. Tang, L. He, L. Chang, M. Montazeri, G. Yu, W. Jiang, T. Nie, R. N. Schwartz, Y. Tserkovnyak, K. L. Wang, *Nat. Mater.* **2014**, *13*, 699.
[11] A. R. Mellnik, J. S. Lee, A. Richardella, J. L. Grab, P. J. Mintun, M. H. Fischer, A. Vaezi, A. Manchon, E.-A. Kim, N. Samarth, D. C. Ralph, *Nature* **2014**, *511*, 449.
[12] D. MacNeill, G. M. Stiehl, M. H. D. Guimaraes, R. A. Buhrman, J. Park, D. C. Ralph, *Nat. Phys.* **2017**, *13*, 300.
[13] M. H. D. Guimarães, G. M. Stiehl, D. MacNeill, N. D. Reynolds, D. C. Ralph, *Nano Lett.* **2018**, *18*, 1311.
[14] Q. Xie, W. Lin, B. Yang, X. Shu, S. Chen, L. Liu, X. Yu, M. B. H. Breese, T. Zhou, M. Yang, Z. Zhang, S. Wang, H. Yang, J. Chai, X. Han, J. Chen, *Adv. Mater.* **2019**, *31*, 1900776.
[15] A. S. Patri, K. Hwang, H. Lee, Y. B. Kim, *Sci. Rep.* **2018**, *8*, 8052.
[16] Z. Fang, N. Nagaosa, K. S. Takahashi, A. Asamitsu, R. Mathieu, T. Ogasawara, H. Yamada, M. Kawasaki, Y. Tokura, K. Terakura, *Science* **2003**, *302*, 92.
[17] R. Mathieu, A. Asamitsu, H. Yamada, K. S. Takahashi, M. Kawasaki, Z. Fang, N. Nagaosa, Y. Tokura, *Phys. Rev. Lett.* **2004**, *93*, 016602.
[18] W. Lu, W. Song, P. Yang, J. Ding, G. M. Chow, J. S. Chen, *Sci. Rep.* **2015**, *5*, 10245.
[19] A. Grutter, E. A. F. Wong, M. Liberati, A. Vailionis, Y. Suzuki, *Appl. Phys. Lett.* **2010**, *96*, 082509.
[20] M. Ziese, I. Vrejoiu, D. Hesse, *Phys. Rev. B* **2010**, *81*, 184418.
[21] Q. Gan, R. A. Rao, C. B. Eom, J. L. Garrett, M. Lee, *Appl. Phys. Lett.* **1998**, *72*, 978.
[22] A. T. Zayak, X. Huang, J. B. Neaton, K. M. Rabe, *Phys. Rev. B* **2008**, *77*, 214410.
[23] A. Herklotz, M. Kataja, K. Nenkov, M. D. Biegalski, H.-M. Christen, C. Deneke, L. Schultz, K. Doerr, *Phys. Rev. B* **2013**, *88*, 144412.
[24] S. Lin, Q. Zhang, M. A. Roldan, S. Das, T. Charlton, M. R. Fitzsimmons, Q. Jin, S. Li, Z. Wu, S. Chen, H. Guo, X. Tong, M. He, C. Ge, C. Wang, L. Gu, K. Jin, E. Guo, *Phys. Rev. Appl.* **2020**, *13*, 034033.
[25] W. Lu, W. D. Song, K. He, J. Chai, C. Sun, G. Chow, J. Chen, *J. Appl. Phys.* **2013**, *113*,063901.
[26] Q. Qin, W. Song, S. He, P. Yang, J. Chen, *J. Phys. D: Appl. Phys.* **2017**, *50*, 215002.
[27] M. C. Langner, C. L. S. Kantner, Y. H. Chu, L. M. Martin, P. Yu, J. Seidel, R. Ramesh, J. Orenstein, *Phys. Rev. Lett.* **2009**, *102*, 177601.
[28] G. Koster, L. Klein, W. Siemons, G. Rijnders, J. S. Dodge, C. B. Eom, D. H. A. Blank, M. R. Beasley, *Rev. Mod. Phys.* **2012**, *84*, 253.
[29] M. W. Haverkort, I. S. Elfimov, L. H. Tjeng, G. A. Sawatzky, A. Damascelli, *Phys. Rev. Lett.* **2008**, *101*, 026406.
[30] P. Jadaun, L. F. Register, S. K. Banerje, *Proc. Natl. Acad. Sci. USA* **2020**, *117*, 11878.
[31] J. Zhou, X. Shu, Y. Liu, X. Wang, W. Lin, S. Chen, L. Liu, Q. Xie, T. Hong, P. Yang, B. Yan, X. Han, J. Chen, *Phys. Rev. B* **2020**, *101*, 184403.
[32] L. Hao, D. Meyers, H. Suwa, J. Yang, C. Frederick, T. R. Dasa, G. Fabbris, L. Horak, D. Kriegner, Y. Choi, J.-W. Kim, D. Haskel, P. J. Ryan, H. Xu, C. D. Batista, M. P. M. Dean, J. Liu, *Nat. Phys.* **2018**, *14*, 806.
[33] L. Chen, C. Xu, H. Tian, H. Xiang, J. Íñiguez, Y. Yang, L. Bellaiche, *Phys. Rev. Lett.* **2019**, *122*, 247701.
[34] D. Yi, Y. Wang, O. M. J. van't Erve, L. Xu, H. Yuan, M. J. Veit, P. P. Balakrishnan, Y. Choi, A. T. N'Diaye, P. Shafer, E. Arenholz, A. Grutter, H. Xu, P. Yu, B. T. Jonker, Y. Suzuki, *Nat. Commun.* **2020**, *11*, 902.
[35] M. S. Saleem, B. Cui, C. Song, Y. Sun, Y. Gu, R. Zhang, M. U. Fayaz, X. Zhou, P. Werner, S. S. P. Parkin, F. Pan, *ACS Appl. Mater. Interfaces* **2019**, *11*, 6581.
[36] Y. Ou, Z. Wang, C. S. Chang, H. P. Nair, H. Paik, N. Reynolds, D. C. RalphDavid, A. MullerDarrell, G. SchlomRobert, A. Buhrman, *Nano Lett.* **2019**, *19*, 3663.
[37] L. Liu, Q. Qin, W. Lin, C. Li, Q. Xie, S. He, X. Shu, C. Zhou, Z. Lim, J. Yu, W. Lu, M. Li, X. Yan, S. J. Pennycook, J. Chen, *Nat. Nanotechnol.* **2019**, *14*, 939.
[38] T. Nan, T. J. Anderson, J. Gibbons, K. Hwang, N. Campbell, H. Zhou, Y. Q. Dong, G. Y. Kim, D. F. Shao, T. R. Paudel, N. Reynolds, X. J. Wang, N. X. Sun, E. Y. Tsymbal, S. Y. Choi, M. S. Rzchowski, Y. B. Kim, D. C. Ralph, C. B. Eom, *Proc. Natl. Acad. Sci. USA* **2019**, *116*, 16186.
[39] L. Zhu, L. Zhu, M. Sui, D. C. Ralph1, R. A. Buhrman, *Sci. Adv.* **2019**, *5*, 8025.
[40] W. Lu, Y. P. Yang, W. D. Song, G. M. Chow, J. S. Chen, *Phys. Rev. B* **2013**, *88*, 214115.
[41] P. Yang, H. Liu, Z. Chen, L. Chen, J. Wang, *J. Appl. Crystallogr.* **2014**, *47*, 402.
[42] A. F. Marshall, L. Klein, J. S. Dodge, C. H. Ahn, J. W. Reiner, L. Mieville, L. Antagonazza, A. Kapitulnik, T. H. Geballe, M. R. Beasley, *J. Appl. Phys.* **1999**, *85*, 4131.
[43] V. Tshitoyan, C. Ciccarelli, A. P. Mihai, M. Ali, A. C. Irvine, T. A. Moore, T. Jungwirth, A. J. Ferguson, *Phys. Rev. B* **2015**, *92*, 214406.
[44] C. O. Avci, K. Garello, M. Gabureac, A. Ghosh, A. Fuhrer, S. F. Alvarado, P. Gambardella, *Phys. Rev. B* **2014**, *90*, 224427.
[45] S. Karimeddiny, J. A. Mittelstaedt, R. A. Buhrman, D. C. Ralph, *Phys. Rev. Appl.* **2020**, *14*, 024024.
[46] R. Itoh, Y. Takeuchi, S. DuttaGupta, S. Fukami, H. Ohno, *Appl. Phys. Lett.* **2019**, *115*, 242404.
[47] C.-F. Pai, Y. Ou, L. H. Vilela-Leão, D. C. Ralph, R. A. Buhrman, *Phys. Rev. B* **2015**, *92*, 064426.
[48] A. Bose, J. N. Nelson, X. S. Zhang, P. Jadaun, R. Jain, D. G. Schlom, D. C. Ralph, D. A. Muller, K. M. Shen, R. A. Buhrman, *ACS Appl. Mater. Interfaces* **2020**, *12*, 55411.
[49] W. Zhang, W. Han, X. Jiang, S.-H. Yang, S. S. P. Parkin, *Nat. Phys.* **2015**, *11*, 496.
[50] D. I. Woodward, I. M. Reaney, *Acta Crystallogr., Sect. B: Struct. Sci.* **2005**, *61*, 387.
[51] B. J. Kennedy, B. A. Hunter, *Phys. Rev. B* **1998**, *58*, 653.

© 2021 Wiley-VCH GmbH

15214095, 2021, 30, Downloaded from https://advanced.onlinelibrary.wiley.com/doi/10.1002/adma.202007114 by Westlake University, Wiley Online Library on [16/10/2026]. See the Terms and Conditions (https://onlinelibrary.wiley.com/terms-and-conditions) on Wiley Online Library for rules of use; OA articles are governed by the applicable Creative Commons License